
VOLUME 333 ISSUE 10
12 MAY 2014
ISSN 0022-460X
ELSEVIER
JOURNAL OF SOUND AND VIBRATION
Available online at www.sciencedirect.com
ScienceDirect

Journal of Sound and Vibration 333 (2014) 2759–2773

Contents lists available at ScienceDirect

Journal of Sound and Vibration

journal homepage: www.elsevier.com/locate/jsvi

A chiral elastic metamaterial beam for broadband vibration suppression

R. Zhu [a], X.N. Liu [b], G.K. Hu [b], C.T. Sun [c], G.L. Huang [a,*]

[a] *Department of Systems Engineering, University of Arkansas at Little Rock, Little Rock, AR 72204, USA*
[b] *School of Aerospace Engineering, Beijing Institute of Technology, Beijing 100081, China*
[c] *School of Aeronautics and Astronautics, Purdue University, West Lafayette, IN 47907, USA*

ARTICLE INFO

Article history:
Received 17 April 2013
Received in revised form
6 December 2013
Accepted 10 January 2014
Handling Editor: G. Degrande
Available online 5 February 2014

ABSTRACT

One of the significant engineering applications of the elastic metamaterial (EMM) is for low-frequency vibration attenuation because of its unusual low-frequency bandgap behavior. However, the forbidden gap from many existing EMMs is usually of narrow bandwidth which limits their practical engineering applications. In this paper, a chiral-lattice-based EMM beam with multiple embedded local resonators is suggested to achieve broadband vibration suppression without sacrificing its load-bearing capacity. First, a theoretical beam modeling is suggested to investigate bandgap behavior of an EMM beam with multiple resonators. New passbands due to dynamic interaction between resonators are unpleasantly formed, which become a design barrier for completely broadband vibration suppression. Through vibration attenuation factor analysis of the resonator, an EMM beam with section-distributed resonators is proposed to enable broadband vibration attenuation function. Required unit number of the resonator in each section is quantitatively determined for complete vibration attenuation in a specific frequency range. Finally, the chiral-lattice-based EMM beam is fabricated, and experimental testing of the proposed structure is conducted to validate the design.

1. Introduction

EMMs have gained much attention due to their unique microstructure designs to achieve effective dynamic material properties which cannot be observed in nature [1]. The working principle of the EMM is to use man-made microstructures (local resonators) on a scale much less than its working wavelength. Therefore, low-frequency bandgap can be observed in the EMM with small dimensions, within which the wave/vibration energy cannot propagate. The unusual low-frequency bandgap in such composite was explained by the negative effective mass density through equivalent discrete mass-spring systems [2–5].

One of the significant engineering applications of the EMM is to achieve the low-frequency vibration attenuation. Different from the Bragg scattering mechanism in phononic crystals [6,7], the locally resonant (LR) mechanism could be easily tuned through proper microstructure design, and low-frequency vibration energy could be quickly attenuated within only a small amount of the periodic microstructures [8]. Therefore, no gigantic meta-structure is needed to shield the structural subject from the low-frequency vibration or wave loading. Engineering structures such as rods, beams and plates

* Corresponding author. Tel.: +1 501 683 7522; fax: ++1 501 569 8698.
E-mail address: glhuang@ualr.edu (G.L. Huang).

0022-460X/$ - see front matter © 2014 Elsevier Ltd. All rights reserved.
http://dx.doi.org/10.1016/j.jsv.2014.01.009

with desired LR microstructure designs were implemented for vibration suppression. Xiao et al. [9] investigated wave propagation and vibration transmission in elastic rods containing periodically attached multi-degree-of-freedom spring-mass resonators. Yu et al. [10] studied the flexural wave propagation in a beam with many spring-mass subsystems as bending wave absorbers. Chen et al. [11] analytically and experimentally studied the behavior of bending wave propagation in a sandwich beam with internal resonators. However, the forbidden gap from the current EMM design is usually of narrow bandwidth, which significantly limits its potential engineering applications. To address this problem, bandgaps in acoustic metamaterials with multi-resonators were investigated [12]. It was found that the bandgaps can be tuned by varying physical parameters of internal resonators. Pai [13] theoretically demonstrated that the longitudinal broadband wave absorption can be achieved in a bar structure with distributed absorbers related to different bandgap frequency ranges in different sections. Based on the study, a metamaterial beam was also suggested to achieve broadband vibration absorption [14]. Similarly, flexural wave propagation in the beam consisting of multiple damped spring-mass resonators with slightly different resonant frequencies was also investigated by Xiao et al. [15]. Broader bandgaps were found at frequencies both below and around the Bragg condition. A chiral-lattice-based metacomposite beam was recently proposed by integrating periodic chiral lattice with LR inclusions for low-frequency vibration attenuation applications [16]. The vibration attenuation function was demonstrated through the numerical analysis of the band diagram. The major advantage of the proposed beam is that the significant vibration attenuation is localized within the structure, which requires no additional structural components. Additionally, the chiral structure beam can still be made from stiff and high strength materials so as not to sacrifice the load-bearing capacity. To accomplish the chiral-lattice-based EMM for vibration attenuation in a broad frequency regime, the EMM beam with multiple inner resonators should be properly designed and the experimental validation of the design should be conducted.

In this paper, a chiral-lattice-based EMM beam with multiple local resonators is numerically and experimentally studied for the broadband vibration suppression by utilizing their individual bandgaps. First, based on the Timoshenko beam theory (TBT) and transfer matrix method (TMM), theoretical modeling of an EMM beam with multiple local resonators is performed for vibration analysis. The undesirable new passbands are observed due to dynamic interaction between the different resonators, which become a major design barrier to form complete vibration attenuation in a desired frequency regime. Through vibration attenuation factor analysis, a section-distributed design of multiple local resonators is suggested to achieve completely broadband vibration suppression and required unit number of the resonator in each section is quantitatively determined. Finally, the chiral-lattice-based EMM beam is fabricated, and experimental frequency response testing is conducted to validate the proposed design as well as the theoretical modeling.

2. Bending vibration in a beam with multiple local resonators

The vibration band structure of a beam with a single LR structure has been investigated based on the transfer matrix theory [17]. In the study, to form a broad forbidden band, we implement this method to obtain the band structure of the EMM beam with multiple local resonators. Attention will be paid on the understanding of dynamic interaction among different local resonators and its effects on vibration transmission. To clearly illustrate the problem, a simple model of the beam with multiple LR units is studied as shown in Fig. 1a. Each unit consists of s subsystems in which mass-spring resonators are attached to the beam at a spacing of a along x direction. Each subsystem consists of two parts, beam segment and local resonator, which is represented by an elastic spring k and a mass m_j, $j = 1, 2, 3, \ldots s$, as shown in Fig. 1b. The lattice constant of the periodic system is denoted as $b = sa$. The x axis of the coordinate system is along the central line of the beam.

The governing equation of the free bending vibration of a Timoshenko beam can be written as follows:

$$\frac{EI}{\rho\overline{A}}\frac{\partial^4 v(x,t)}{\partial x^4} - \left(\frac{\rho I}{\rho\overline{A}} + \frac{EI}{\kappa G\overline{A}}\right)\frac{\partial^4 v(x,t)}{\partial x^2 \partial t^2} + \frac{\partial^2 v(x,t)}{\partial t^2} + \frac{\rho I}{\kappa G\overline{A}}\frac{\partial^4 v(x,t)}{\partial t^4} = 0, \tag{1}$$

where ρ, E, and G are the density, Young's modulus, and shear modulus, respectively; $\overline{A}$ is the cross-section area; κ is the Timoshenko shear coefficient; I is the cross-section-area moment of inertia about the axis perpendicular to x and y axes. Unlike Euler–Bernoulli beam theory which neglects shear deformation, Timoshenko beam with rotary inertia considers the deformation of the beam cross-section, therefore it is more suitable for short beams i.e., those with relatively high cross-sections compared with their lengths, especially when they are subjected to significant shear forces. Since only the steady-state response will be considered in this section, the time factor $e^{i\omega t}$, which applies to all the field variables, will be suppressed. Therefore, the amplitude $Y(x)$ of the bending displacement $v(x,t)$ can be determined as [18,19]

$$Y(x) = Ak_1^{-3}e^{q_1 x} + Bk_2^{-3}e^{q_2 x} + Ck_3^{-3}e^{q_3 x} + Dk_4^{-3}e^{q_4 x}, \tag{2}$$

where

$$q_r = (-1)^{[r/2]}\sqrt{[\overline{\alpha} + (-1)^r\sqrt{\overline{\alpha}^2 + 4\overline{\beta}}]/2}, \quad r = 1, \ldots, 4, \ \overline{\alpha} = -\frac{\rho\omega^2}{E} - \frac{\rho\omega^2}{\kappa G} \text{ and } \overline{\beta} = \frac{\rho\overline{A}\omega^2}{EI} - \frac{\rho^2\omega^4}{E\kappa G}, \ \left[\frac{r}{2}\right]$$

is the largest integer less than $r/2$. In Eq. (2), q_r ($r = 1, 2, 3, 4$) represent the wavenumbers of the two lowest vibration modes along two directions (positive and negative x directions).

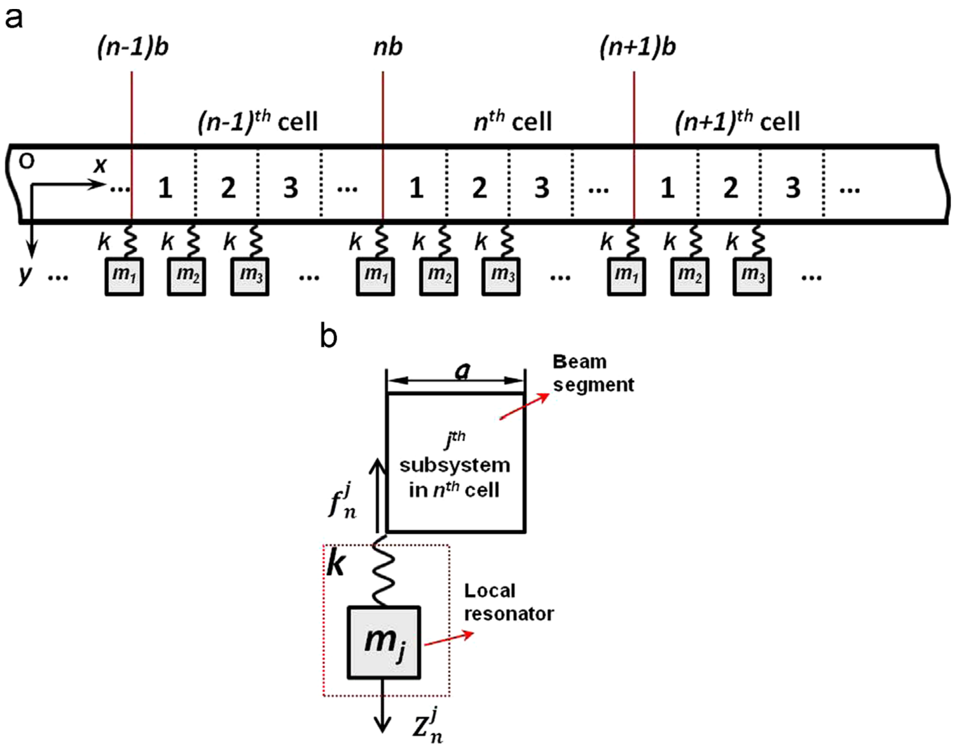

Fig. 1. (a) The model of an EMM beam with multiple LR units. (b) The jth subsystem in nth unit cell with applied forces.

For the jth subsystem in the nth cell as shown in Fig. 1b, $Y(x)$ can be rewritten as

$$Y_n^j(x) = A_n^j q_1^{-3} e^{q_1(x-nb)} + B_n^j q_2^{-3} e^{q_2(x-nb)} + C_n^j q_3^{-3} e^{q_3(x-nb)} + D_n^j q_4^{-3} e^{q_4(x-nb)}, \tag{3}$$

where $nb+(j-1)a \le x \le nb+ja$ and $j=1, 2, 3, \ldots s$. The equilibrium condition for the jth mass-spring resonator m_j in the nth cell along the vertical direction is

$$F_n^j - m_j \ddot{Z}_n^j = 0, \tag{4}$$

where F_n^j is the interactive force between the mass-spring local resonator and the beam segment, Z_n^j is the displacement of the jth mass-spring local resonator at the position $x=nb+(j-1)a$. Then, the force F_n^j can be calculated as

$$F_n^j = k[Y_n^j(ja-a) - Z_n^j], \tag{5}$$

where k is the spring constant. Substituting Eqs. (5) into (4) leads to

$$Z_n^j = \frac{k}{k - m_j\omega^2} Y_n^j(ja-a). \tag{6}$$

Applying the continuity conditions of displacement, displacement gradient, bending moment, and shear force at the interface between jth and $(j-1)$th subsystems in the nth cell, we have

$$Y_n^j[(j-1)a] = Y_n^{j-1}[(j-1)a], \tag{7a}$$

$$Y_n'^j[(j-1)a] = Y_n'^{j-1}[(j-1)a], \tag{7b}$$

$$EIY_n''^j[(j-1)a] = EIY_n''^{j-1}[(j-1)a], \tag{7c}$$

$$EIY_n'''^j[(j-1)a] - F_n^j = EIY_n'''^{j-1}[(j-1)a]. \tag{7d}$$

Substituting Eqs. (3) and (6) into (7), the continuity conditions can be expressed in the matrix form as

$$\mathbf{K}_j \boldsymbol{\psi}_n^j = \mathbf{H}_j \boldsymbol{\psi}_n^{j-1}, \tag{8}$$

where

$$\mathbf{K}_j = \begin{bmatrix} q_1^{-3}e^{q_1(j-1)a} & q_2^{-3}e^{q_2(j-1)a} & q_3^{-3}e^{q_3(j-1)a} & q_4^{-3}e^{q_4(j-1)a} \\ q_1^{-2}e^{q_1(j-1)a} & q_2^{-2}e^{q_2(j-1)a} & q_3^{-2}e^{q_3(j-1)a} & q_4^{-2}e^{q_4(j-1)a} \\ q_1^{-1}e^{q_1(j-1)a} & q_2^{-1}e^{q_2(j-1)a} & q_3^{-1}e^{q_3(j-1)a} & q_4^{-1}e^{q_4(j-1)a} \\ (1+\overline{F}_j q_1^{-3})e^{q_1(j-1)a} & (1+\overline{F}_j q_2^{-3})e^{q_2(j-1)a} & (1+\overline{F}_j q_3^{-3})e^{q_3(j-1)a} & (1+\overline{F}_j q_4^{-3})e^{q_4(j-1)a} \end{bmatrix},$$

$$\mathbf{H}_j = \begin{bmatrix} q_1^{-3}e^{q_1[(j-1)a]} & q_2^{-3}e^{q_2[(j-1)a]} & q_3^{-3}e^{q_3[(j-1)a]} & q_4^{-3}e^{q_4[(j-1)a]} \\ q_1^{-2}e^{q_1[(j-1)a]} & q_2^{-2}e^{q_2[(j-1)a]} & q_3^{-2}e^{q_3[(j-1)a]} & q_4^{-2}e^{q_4[(j-1)a]} \\ q_1^{-1}e^{q_1[(j-1)a]} & q_2^{-1}e^{q_2[(j-1)a]} & q_3^{-1}e^{q_3[(j-1)a]} & q_4^{-1}e^{q_4[(j-1)a]} \\ e^{q_1[(j-1)a]} & e^{q_2[(j-1)a]} & e^{q_3[(j-1)a]} & e^{q_4[(j-1)a]} \end{bmatrix},$$

$$\boldsymbol{\psi}_n^j = \begin{bmatrix} A_n^j \\ B_n^j \\ C_n^j \\ D_n^j \end{bmatrix}, \quad \overline{F}_j = \frac{-1}{EI}\frac{m_j k \omega^2}{k - m_j\omega^2}.$$

Based on Eq. (8), the wave transfer relation between the nth cell and $(n-1)$th cell can be given as

$$\boldsymbol{\psi}_n = \mathbf{T}\boldsymbol{\psi}_{n-1}, \tag{9}$$

where $\mathbf{T} = \mathbf{K}_s^{-1}\mathbf{H}_s \ldots \mathbf{K}_1^{-1}\mathbf{H}_1$ is the transfer matrix between the two cells [20]. It should be mentioned that the TMM based on the coefficient of $Y(x)$ can obtain the same result as that obtained by using the TMM based on the global solution, such as: displacement, displacement gradient, bending moment and shear force.

For an infinite periodic EMM beam, Bloch theorem can be applied as

$$\boldsymbol{\psi}_n = e^{iqb}\boldsymbol{\psi}_{n-1}, \tag{10}$$

where q is the wavenumber in the x direction. Inserting Eq. (9) into (10) yields the eigen-value problem:

$$|\mathbf{T} - e^{iqb}\mathbf{I}| = 0, \tag{11}$$

from which the band structure of the EMM beam can be determined.

Fig. 2a shows the band structure of the EMM beam consisting of two periodic resonant subsystems with masses m_1 and m_2. The material and geometrical parameters used in the calculation are listed in Table 1. In the figure, $q^* = (qb/\pi)$ is the normalized wavenumber along the x direction, the normalized frequency is defined as $f^* = (f/f_0)$, where $f_0 = (1/2\pi)\sqrt{k/m_1}$. For the sake of comparison, the band structure of the EMM beams with the single periodic resonator (m_1 or m_2), are also depicted in Fig. 2b and c, respectively. Comparing with the bandgap frequency ranges (1, 1.55) of the EMM beam with the resonant mass m_1 and (0.50, 1.29) of the EMM beam with the resonant mass m_2, bandgap frequency range of the EMM beam

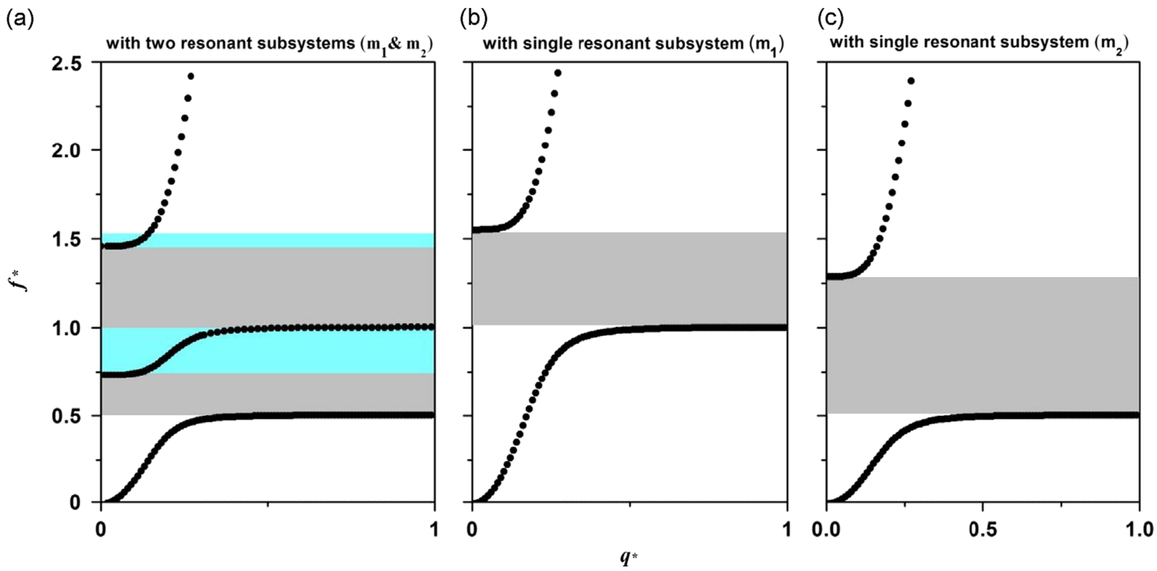

Fig. 2. Band structures of the EMM beam units with (a) a single resonator m_1; (b) a single resonator m_2; and (c) two resonators (m_1 and m_2).

Table 1
Geometrical and material parameters for the broadband EMM beam.

Geometrical parameters		Material parameters	
a	75 mm	Mass density of the beam, ρ	2600 kg m^{-3}
b	150 mm	Young's modulus of the beam, E	70 GPa
$\overline{A}$	160.2 mm^2	Shear modulus of the beam, G	27 GPa
I	5968 mm^4	Timoshenko shear coefficient, κ	0.925
		Spring constant k	165,000 N m^{-1}
		Mass, m_1	0.0437 kg
		Mass, m_2	0.1748 kg

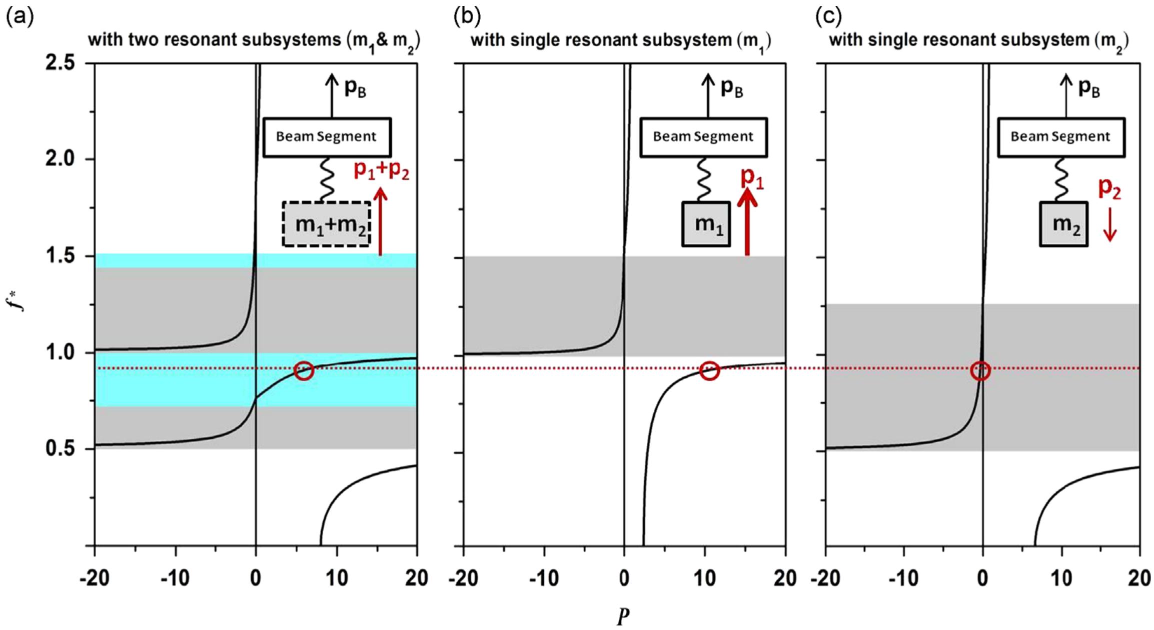

Fig. 3. Linear momentum ratios of the beam units with (a) a single resonator m_1; (b) a single resonator m_2; and (c) two resonators (m_1 and m_2). (For interpretation of the references to color in this figure, the reader is referred to the web version of this article.)

with the two resonant masses is increased to (0.50, 1.46), which seems to be the linear summation of bandgap frequency ranges of the EMM beams with the individual resonator. However, two new passbands are unexpectedly formed at the frequency ranges (0.73, 1) and (1.46, 1.55). The first new passband (0.73, 1) locates within the acoustic passband of the resonant mass m_1 but the forbidden band of the resonant mass m_2. In contrast, the second new passband (1.46, 1.55) locates within the forbidden band of the resonant mass m_1 but the optical passband of the resonant mass m_2. The new passbands are undesirable to form completely broadband vibration attenuation and should be eliminated.

To understand new passband's formation mechanism, detailed linear momentum analysis within the unit cell is conducted to quantitatively illustrate the dynamic interaction between different resonators, because linear momentum in the host beam segment and linear momentum in the resonators, which are proportional to their inertia forces, could provide a clear physical explanation about the generation of the new passband. In the study, the linear momentum ratio $P=(\mathbf{p}_{\text{total}}/\mathbf{p}_B)$ is defined as a physical parameter to reflect the vibration behavior, where the total linear momentum in the unit cell is defined as $\mathbf{p}_{\text{total}}=\mathbf{p}_B+\sum_{j=1}^{2}\mathbf{p}_j$, and the linear moment in the host beam and the resonator j are defined as $\mathbf{p}_B=\int_0^b \rho\overline{A}\dot{\mathbf{v}}(x)dx$ and $\mathbf{p}_j=m_j\dot{\mathbf{Z}}_n^j$, $j=1,\ 2$, respectively. It is well known that when the total linear momentum is out of phase with the linear momentum of the host beam, the linear momentum ratio P becomes a negative value. Therefore, the vibration cannot transmit through the EMM beam and a bandgap is generated. On the other hand, when the total linear momentum is in phase with the linear momentum of the host beam, P will be a positive value and a vibration passband is then guaranteed. Fig. 3 shows the linear momentum ratio P of the EMM beam with two different resonant masses and those of the EMM beam with the single resonant mass m_1 or m_2, respectively. Gray shaded areas show the bandgaps and blue shaded areas indicate the new passbands. For example, at the frequency $f^*=0.9$ in the first new passband, $\mathbf{p}_2$, the linear momentum of the local resonant mass m_2, is out of phase with $\mathbf{p}_B$ while $\mathbf{p}_1$, the linear momentum of the local resonant mass m_1, is in phase with $\mathbf{p}_B$. Therefore, m_2 is moving along opposite direction with the beam segment and m_1 is moving along the same direction with the beam, as illustrated in Fig. 3. However, the amplitude of $\mathbf{p}_1$ is larger than that of $\mathbf{p}_2$ at this frequency, therefore, the total momentum in the unit cell is still in phase with that of the host beam segment, which gives a clear explanation about the generation of the new passband in the EMM beam. Based on this understanding, the newly formed passbands, as shown in Fig. 2, can be quantitatively determined through the positive/negative value of the linear momentum ratio P. It should be mentioned that the dynamic interaction between different resonators could be tuned through careful design of multiple resonators. However, in order to achieve complete low-frequency vibration suppression, this dynamic interaction is undesirable and should be avoided for practical engineering application.

3. Section design of multiple local resonators

In the study, a section design of multiple local resonators in the finite EMM beam is proposed for broadband vibration attenuation by eliminating the dynamic interaction between different resonators in the unit cell, and its resulting new passbands. Each section is composed of a finite unit number of particular resonator to completely attenuate vibration energy in a certain frequency range. One of the most fundamental issues in this design is to determine required unit number of the resonator in each section to fully attenuate the vibration energy in the specified frequency range. Harmonic bending simulation of the finite EMM beam with finite local resonators (X units) is conducted. Based on the transfer matrix $\mathbf{T}^X$, in Eq. (9), frequency response function (FRF) of the finite beam [21], which is the ratio of the amplitude of the out-of-plane acceleration at the right end to the amplitude of the out-of-plane excitation force at the left end, can be obtained by setting the boundary conditions as [17,22]

$$EIY_0^{''1}(0) = 0, \tag{12a}$$

$$EIY_0^{'''1}(0) = \hat{F}_0, \tag{12b}$$

$$EIY_X^{''s}(b) = 0, \tag{12c}$$

$$EIY_X^{'''s}(b) = 0, \tag{12d}$$

where the harmonic excitation force, $\hat{F}_0$, is applied to the left end of the finite beam along transverse direction and the right end of the beam is assumed to be free.

Fig. 4a and b show FRFs of the finite EMM beams with the resonant masses m_1 and m_2, respectively. In both figures, the finite EMM beams with 6, 11 and 16 units of the resonator are studied. The shaded areas in the figures indicate the predicted bandgaps of the infinite EMM beam based on the TBT model. It can be found that the vibration attenuation frequency region becomes wider and converges to a stable frequency region with the increase of the unit number of the resonator. Therefore, sufficient resonator units should be determined to function as a section in the finite EMM beam to completely attenuate the vibration energy in the desired frequency range to match bandgap prediction of the infinite EMM beam. Also, it is noticed that the required unit number of the resonator could be tuned through the change of physical parameters of the local resonator, such as resonant mass.

For any frequency within the bandgap of the EMM beam containing finite resonator units, if substituted in the dispersion relation Eq. (11), a wavenumber yields in the complex form $q(\omega)=\alpha+\beta i$. Then, a vibration attenuation factor of the finite EMM beam can be defined as $e^{-\beta^* n}$, where the vibration attenuation coefficient $\beta^* = \beta b$ is the normalized imaginary part of the wavenumber and n is the unit number of the resonator. In this study, $e^{-\beta^* n} = 0.01$ is chosen as a sufficient vibration attenuation threshold for the finite EMM beam and the designed vibration attenuation frequency region (ω_1, ω_2) by the finite EMM beam is assumed to cover 90 percent of the bandgap predicted from the infinite EMM beam. In the study, we focus on the vibration attenuation behavior of the EMM beam at the upper bound frequency ω_2 to meet the defined attention threshold, which require the maximum unit number of the resonator. Fig. 5 shows the function of required unit number of the resonator along the beam direction to achieve complete vibration attenuation in the frequency $\omega=\omega_2$ in

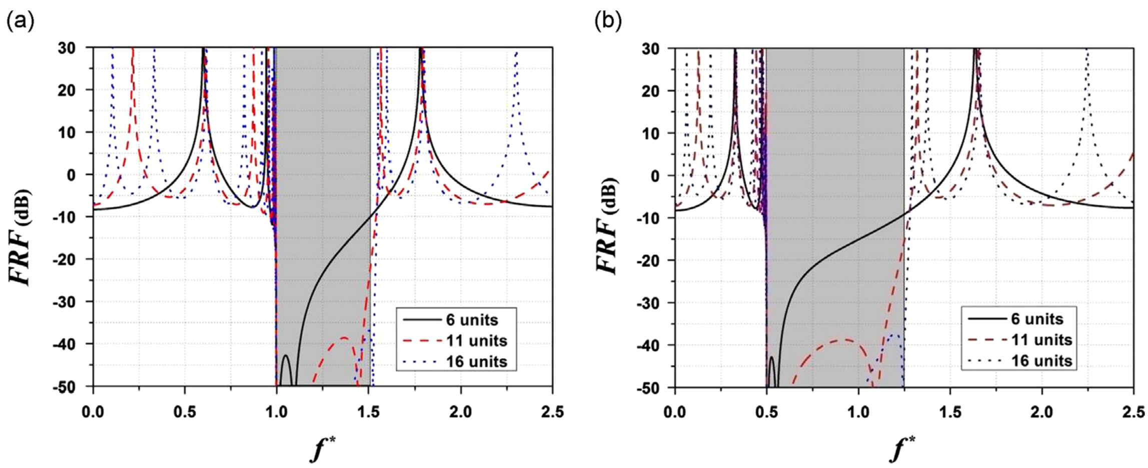

Fig. 4. (a) FRFs of the finite EMM beams with different unit numbers of the resonant mass m_1 and (b) FRFs of the finite EMM beams with different unit numbers of the resonant mass m_2.

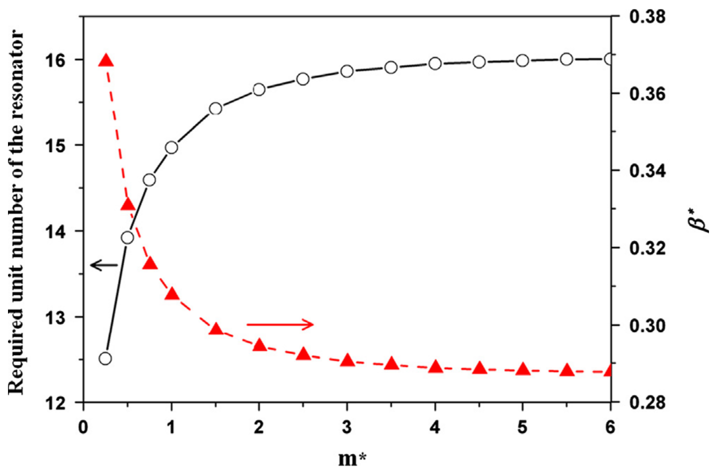

Fig. 5. The required unit number of the resonator and the imaginary part of the wavenumber as functions of the dimensionless resonant mass in the EMM beam.

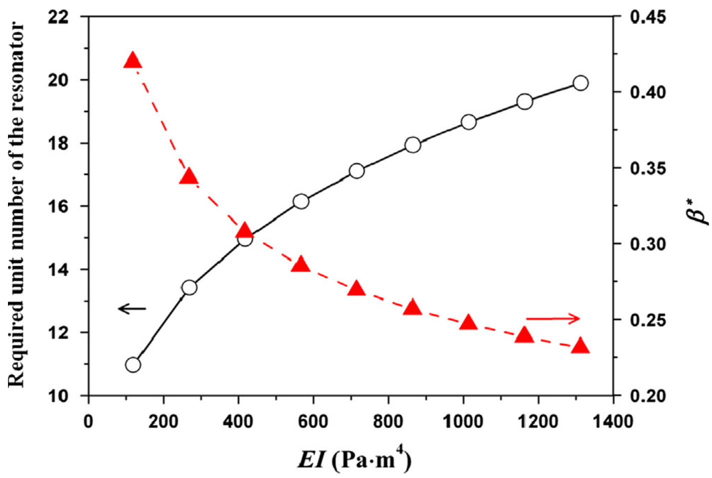

Fig. 6. The required unit number of the resonator and the imaginary part of the wavenumber as functions of bending stiffness of the host beam.

function of the dimensionless resonant mass. In the figure, the normalized mass is defined as $m^* = (m_1/m_0)$, where $m_0 = 0.0437$ kg. The unit dimension of the EMM beam is b=75mm and the spring constant is $k = 165{,}000$ N m^{-1}. It can be found that more unit number of the resonator is needed with the increase of the resonant mass, and 16 resonator units are sufficient for all the considered cases, which is consistent with the previous prediction in Fig. 4. The vibration attenuation coefficient (normalized wavenumber's imaginary part) β^* of the EMM beam in the frequency $\omega = \omega_2$ is also plotted in Fig. 5. It is noticed that the vibration attenuation coefficient of the EMM beam decreases as the value of the resonant mass increases, which means that more resonators along the beam direction are needed to sufficiently attenuate vibration for the EMM beam with larger resonant mass. Fig. 6 shows required unit number of the resonator with the change of flexibility of the host beam. In the figure, geometrical and material properties of the EMM beam are kept the same as they are in Table 1 except for the bending stiffness of the beam. It can be found that the required unit number of the resonator increases as the bending stiffness of the beam increases while the vibration attenuation coefficient, β^*, decreases as the bending stiffness increases. Therefore, the vibration attenuation coefficient of the EMM beam can be used as the beam attenuation factor to determine the required unit number of the resonator.

Finally, to validate the proposed section design, the FRF of a finite beam with two distributed resonator sections is evaluated based on the TMM. Fig. 7 shows the calculated FRF of the proposed finite EMM beam. In the figure, the first section contains 16 resonant units consisting of mass m_1 and the second section contains 16 resonant units consisting of mass m_2. A complete broadband vibration attenuation regime is successfully formed in the normalized frequency range between 0.5 and 1.54 which almost coincides with the linear summation of the bandgap frequency range of EMM beams with resonant mass m_1, (1, 1.55) and the bandgap frequency range of EMM beams with resonant mass m_2, (0.50, 1.29).

4. Experimental testing of the EMM beam

In order to apply the broadband design in the realistic structures, a chiral-lattice-based EMM beam integrated with different section-distributed resonators is fabricated. Chiral lattice is selected due to its excellent capability for load bearing

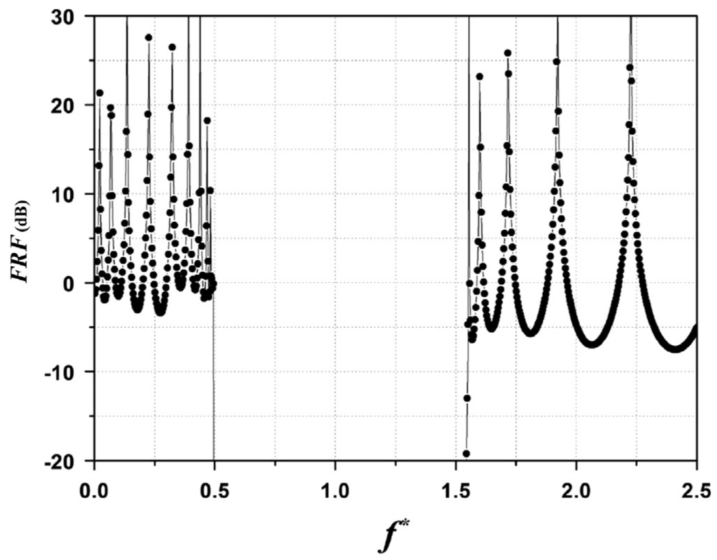

Fig. 7. The FRF of the finite EMM beam with two resonator sections.

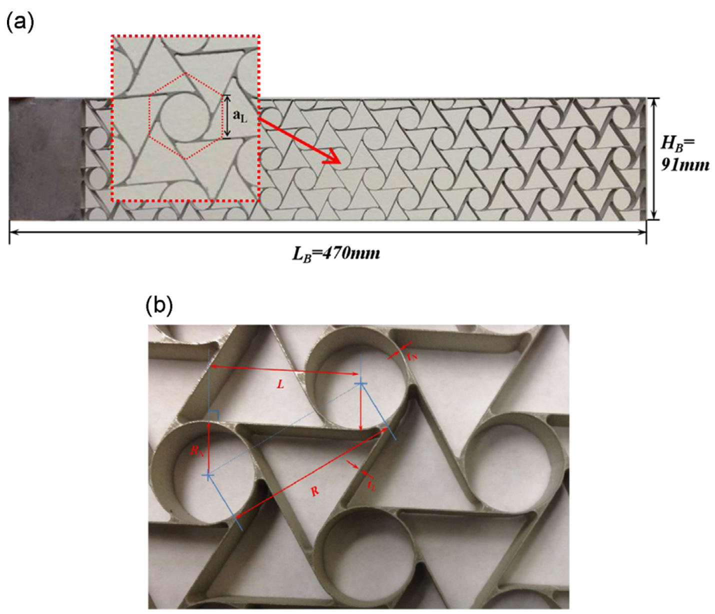

Fig. 8. (a) The fabricated chiral lattice beam and its zoomed unit cell and (b) the topology of the hexagonal chiral lattice.

and feasibility for the inner resonator implantation. The resonators can be implanted into the node circles of the chiral lattice therefore the load-bearing capacity of chiral lattice will not be affected. First, the chiral honeycomb beam is fabricated from an aluminum (Al) beam through a water jet cutter, as shown in Fig. 8a. A unit cell of the chiral lattice is also zoomed in Fig. 8a. In the beam structure, the periodic chiral lattice is sandwiched into a beam frame and the end of each ligament is rigidly linked to the frame. The length of the sandwich beam is $L_B=470$ mm, the total height is $H_B=91$ mm and the height of the chiral layer is $H_C=90$ mm, the width of the beam is $W_B=10$ mm. The wall thickness of the frame is 0.5 mm. The structure contains 16 unit cells in the length direction and 3 unit cells in the height direction. The zoomed picture in Fig. 8b shows the topology of the hexagonal chiral lattice used in the finite beam. The geometrical and material parameters of the chiral lattice beam are listed in Table 2. Then, to form the EMM beam for vibration attenuation, local resonators, made of rubber (Polytek® Poly PT Flex 20 RTV Liquid Rubber, Polytek Development Corp.) coated metal cylinders, are filled in the node circles of the chiral lattices with the help of a supplementary guiding plate, which is used to precisely locate the metal cylinders. Steel cylinders as well as tungsten cylinders with the same geometry, 6.35 mm in diameter and 25.4 mm in height, are used as inclusion cores. The geometrical and material parameters of the local resonators are listed in Table 3.

Fig. 9 shows the experimental set-up of the vibration testing. The chiral EMM beam is fixed on one end and excited by a shaker (LDS V203) which is close to the fixed end. The shaker is powered by a power amplifier (LDS PA25E). White noise excitation signal with bandwidth from 0 to 1000 Hz is generated by the shaker, and the response of the finite chiral EMM beam is captured by an accelerometer, which is attached to the other end of the EMM beam. Both the input signal and the

Table 2
Geometrical and material parameters of the chiral lattice beam.

Geometrical parameters		Material parameters	
Topology parameter	$L/R = 0.82$	Mass density	$2700\ \text{kg m}^{-3}$
Ligament length	$L = 24.6$ mm	Young's modulus	71 GPa
Node radius	$R_n = 8.6\ \text{mm}^2$	Poisson's ratio	0.33
Ligament wall thickness	$t_L = 0.5$ mm		
Node wall thickness	$t_N = 0.5$ mm		
Unit cell size	$a_L = 15$ mm		

Table 3
Geometrical and material parameters of the local resonator.

Geometrical parameters		Material parameters	
Diameter of the metal cylinder	$D_c = 6.35$ mm	Mass density of steel	$7850\ \text{kg m}^{-3}$
Height of the metal cylinder	$H_c = 25.4$ mm	Mass density of tungsten	$15{,}630\ \text{kg m}^{-3}$
		Elastic modulus of the rubber	586 MPa
		Loss tangent of the rubber ($\tan\delta$)	< 0.1

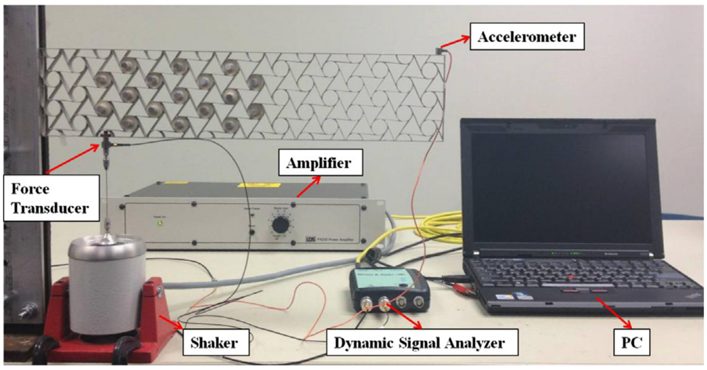

Fig. 9. Experimental set-up of the vibration testing of the EMM beam.

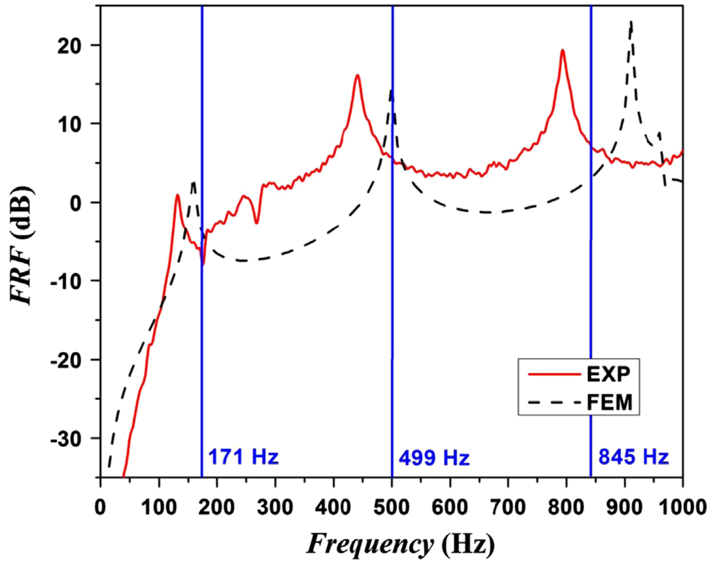

Fig. 10. The FRFs of the chiral lattice beam from the experimental testing and the FE method. The blue vertical lines indicate the calculated natural frequencies from the TBT model. (For interpretation of the references to color in this figure legend, the reader is referred to the web version of this article.)

output signal are recorded by the dynamic signal analyzer (Dactron PHOTON+™). A laptop installed with Data Recorder software is used for the post-processing. The experimental measured FRF is defined as the ratio of the output voltage signal from the accelerometer with respect to the input voltage signal from the force transducer as a function of frequency.

Experimental vibration testing on the chiral lattice beam without local resonators is first performed to validate the experimental set-up of the system. Fig. 10 shows the measured FRF of the chiral lattice beam. For comparison, the FRF calculated from the finite element (FE) method based on the exact geometry of the beam specimen is also depicted in the figure. Both FRF results give close estimation about the first and second natural frequencies of the bending mode. There is a small difference about the third natural frequency prediction from the experimental measurement and the FE method, which can be accounted for errors in specimen manufacturing accuracy control such as: ligament wall thickness. The measured FRF peaks are also compared with the three lowest natural frequencies obtained from the TBT model, which are marked with blue vertical lines in Fig. 10. In the TBT model, the beam specimen is homogenized as a sandwich beam with two Al face sheets, and effective material properties for the core layer are calculated from the chiral lattice structure [16]. The effective bending stiffness (EI) and the effective transverse shear stiffness ($kG\overline{A}$) of the sandwich beam are listed in Table 4 and the detailed derivation can be found in Appendix A. It is noted that the TBT model can give very good prediction about the two lowest natural frequencies, and the small discrepancy for the third natural frequency prediction can be attributed to approximate estimations of the effective properties of the sandwich beam such as the mass of the sandwich beam per unit length, ρA, and the rotary inertia, ρI. In order to improve the accuracy of the TBT model, a model based on the exact geometry of the chiral lattice beam cross section is needed [23], which requires complicated and large computational work and is beyond the interest of this paper. Overall, it is evident that the TBT model is applicable for the current beam. In the following, the proposed experimental set-up and TBT model will be used for the vibration characterization of the finite EMM beam.

Next, vibration testing is conducted on the finite chiral EMM beam. Fig. 11 shows the FRF comparison of the finite EMM beam with 7 resonator units (rubber coated steel cylinders) from both the experimental measurement and FE simulation. Based on the TBT model, bandgap prediction for the infinite chiral EMM beam is also inserted in the shaded area. In the model, the resonators are represented by the effective spring-mass system with effective properties listed in Table 4. The lattice constant is $\sqrt{3}a_L$. The effective masses of the steel and tungsten cylinders are calculated by simply taking products of densities and volumes of the cylinders. The effective spring constant of the rubber coating layer can be numerically determined based on a model of two springs connecting the center mass along the vibration direction as $k^r_{\mathrm{eff}} = F_c/\gamma_c$, where F_c is the restoring force on the outer fixed boundary of the coating layer and γ_c is the applied displacement along the vibration direction [24]. For the resonator in TBT model, which is represented by a single spring connecting the center mass

Table 4
Effective material properties of the chiral lattice, the local resonator and the sandwich beam.

Chiral lattice		Sandwich beam		Local resonator	
Effective mass density	$\rho_{\mathrm{eff}} = 194.75$ kg m^{-3}	Effective bending stiffness	$(EI) = 1662.7$ Pa m^4	Effective mass (steel cylinder)	$m^1_{\mathrm{eff}} = 0.0063$ kg
Effective bulk modulus	$\kappa_{\mathrm{eff}} = 0.01328$ GPa	Effective transverse shear stiffness	$(kG\overline{A}) = 17,360$ Pa m^2	Effective mass (tungsten cylinder)	$m^2_{\mathrm{eff}} = 0.0126$ kg
Effective shear modulus	$\mu_{\mathrm{eff}} = 0.03334$ GPa	Effective rotary inertia	$(\rho I) = 1.736\mathrm{e}^{-4}$ kg m	Effective spring constant	$k_{\mathrm{eff}} = 24892$ N m^{-1}
		Mass per unit length	$(\rho\overline{A}) = 0.2016$ kg m^{-1}		

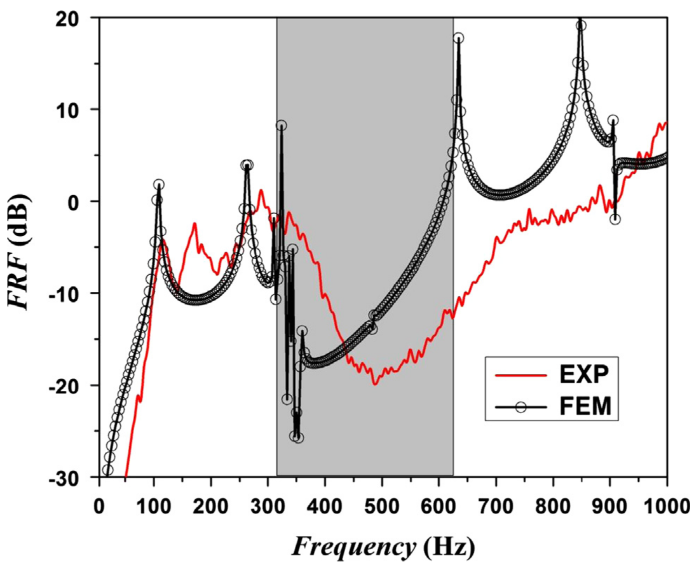

Fig. 11. The FRFs of the finite chiral EMM beam from the experimental testing and the FE method. The shade area indicates the bandgap prediction of the infinite effective EMM beam.

as shown in Fig. 1, the effective spring constant should be equivalent as $k_{\rm eff} = 2k^{r}_{\rm eff}$. Strong vibration attenuation at the low-frequency regime can be observed from both the FE and experimental results. The vibration attenuation frequency region is in good agreement with that by the FE simulation, which is also within the bandgap frequency region predicted by the TBT model (shaded area). As shown in the figure, the FRF amplitude will have a significant drop when the frequency approaches to the resonant frequency (317 Hz) which is the lower boundary of the predicted bandgap. However, the FRF drop obtained from the experimental testing is not as sharp as that from the FE simulation. That is because the FE simulation does not consider damping factor of the rubber coating. It was reported that the vibration attenuation frequency region will be enlarged and the FRF amplitude will be decreased by including material damping factor in the resonator [25]. In the current experimental testing, the resonators (rubber coated steel cylinders) are distributed in a block instead of randomly spacing out through the beam. Numerical simulation has revealed that the resonators can efficiently attenuate vibration if they are distributed in a block with length more than the half-wavelength of the vibration [14].

As discussed in the previous section, to achieve broadband vibration attenuation, sufficient resonator units in each section of the finite EMM beam are needed. To experimentally implement the design, the FRF of the EMM beam with required unit number of the resonator should be first explored. Fig. 12 shows measured FRFs on the finite EMM beam with different units of the resonator (rubber-coated steel cylinders). For the sake of clear demonstration, the FRF of the chiral lattice beam without resonators is also plotted in the figure. From the figure, a clear drop in the FRF corresponding to the local resonance frequency is found for the beam with resonators, while no such FRF drop can be found in the beam without resonators. In addition, vibration attenuation frequency region increases with the increase of the resonant unit number, as expected, and finally converges when the resonant column number is larger than seven. Therefore, for the current resonator (rubber coated steel cylinders), only seven columns are needed to achieve sufficient vibration attenuation in the designed frequency region. Similarly, experimental testing of the finite EMM beam with another resonator (rubber coated tungsten cylinders) is conducted and the finite EMM with eleven resonant columns is needed to obtain the desired vibration attenuation frequency region. The difference in the require column of the resonators is due to the different effective resonant masses calculated from the beams with steel cylinders and tungsten cylinders. According to the previous numerical prediction in Fig. 5, the vibration attenuation coefficient of the beam, β^*, decreases when the resonant mass increases. Therefore, more tungsten cylinders are needed due the larger equivalent resonant mass of the tungsten resonator. This understanding is important since the light weight requirement of a structure is crucial for many engineering applications.

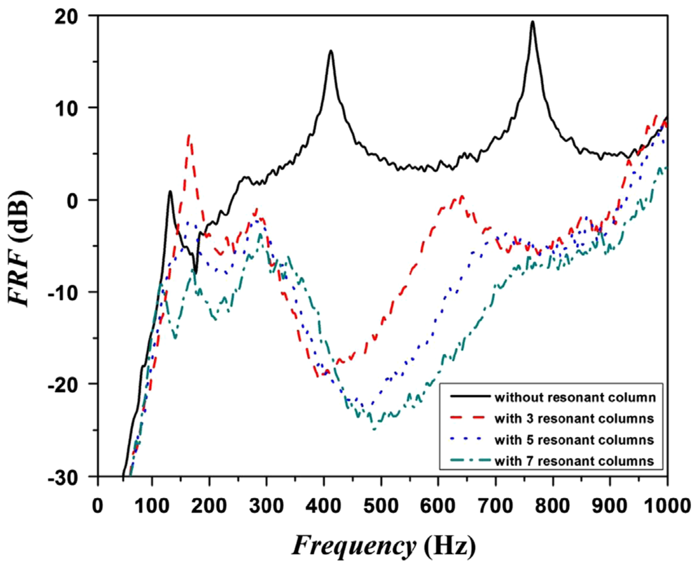

Fig. 12. Experimentally obtained FRFs of the finite EMM beams with different column numbers.

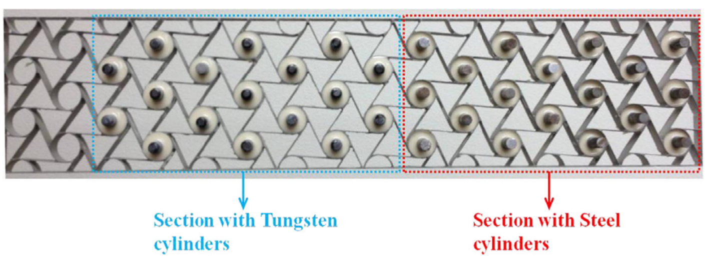

Fig. 13. The finite broadband EMM beam with two resonator sections.

Fig. 13 shows the designed EMM beam specimen with two resonator sections for the broadband vibration attenuation. In the specimen, seven resonant columns made of rubber coated steel cylinders are inserted in the right section of the beam, and seven resonant columns made of rubber coated tungsten cylinders are inserted into the left section of the beam due to the beam dimension limitation. The total weight of the EMM beam increases 155 percent compared with the chiral beam specimen without resonators. The optimization analysis is further needed to make a good trade-off between the weight increase and efficient vibration attenuation ability. The measured FRF of the EMM beam with two sections in Fig. 13 is illustrated in Fig. 14a. For a clear demonstration, the measured FRFs from the EMM beams with seven single resonant columns (rubber-coated steel or tungsten cylinders) are also plotted in the figure. As expected, the vibration attenuation frequency region of the designed EMM beam is located at the frequency range between 210 Hz and 700 Hz, which is very close to the linear summation of the measured vibration attenuation frequency regions of the EMM beams with the individual resonator section. The measured vibration attenuation frequency region is also compared with bandgap predictions of the infinite EMM beams based on the TBT model. In the figure, yellow shaded area indicates the bandgap of the EMM beam with periodic rubber-coated tungsten cylinders and gray shaded area indicates the bandgap of the EMM beam with periodic rubber-coated steel cylinders. It is not surprising that the vibration attenuation frequency region of the EMM beam with two sections can be predicted by overlapping their individual bandgaps. After a close inspection, we found that there is a frequency difference for rubber-coated tungsten cylinders between the measured vibration attenuation

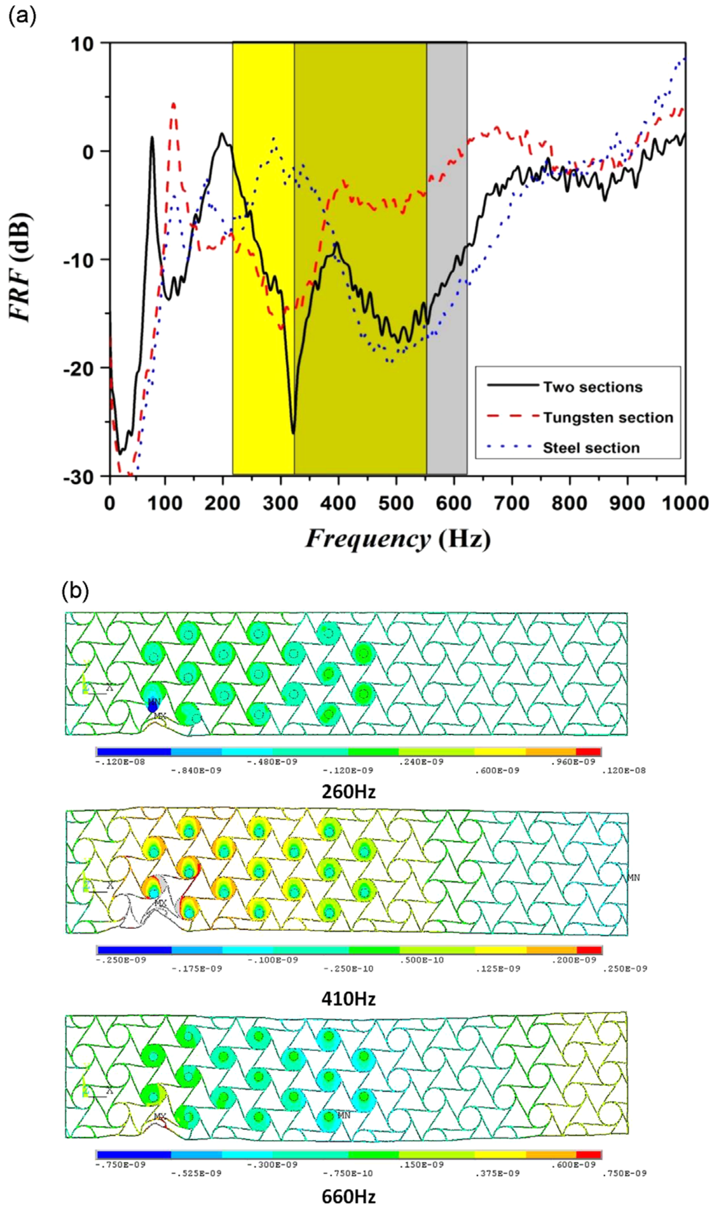

Fig. 14. (a) The measured FRFs of the proposed broadband EMM beam with two sections and the EMM beams with the single section. The shade areas indicate the bandgap predictions of the infinite effective EMM beams. (b) The vibration modes of the EMM beam with seven tungsten resonant columns from the FE simulation at different frequencies. (For interpretation of the references to color in this figure, the reader is referred to the web version of this article.)

frequency region of the finite EMM beam and the bandgap prediction of the infinite EMM beam. The difference is due to the lack of sufficient tungsten resonant units in the finite EMM beam to completely attenuate the vibration energy, as we calculated in the previous section.

To further illustrate this phenomenon, vibration modes of the EMM beam with seven tungsten resonant columns from the FE simulation are demonstrated in Fig. 14b at frequencies 260 Hz, 410 Hz and 660 Hz. It is noted that the vibration decays significantly at 260 Hz, which is very close to the local resonance frequency, and all the vibration energy is trapped in the first two columns of the tungsten resonators. When the frequency approaches to 410 Hz, which is still within the bandgap regime, the resonators does show the out-of-phase motion with respect to the beam. However the motion in the finite resonators is not sufficient enough to attenuate the total vibration energy. This fact can be also reflected in the measured FRF of the EMM beam. A small vibration transmission around the 410 Hz frequency range can be observed as illustrated in Fig. 14a. For the frequency at 660 Hz, which is outside the bandgap regime, the mode shape shows that the resonators have nearly no motion therefore they have small effect on the global motion of the beam. Vibration propagation occurs mostly through the bending deformation of the lattice ribs.

5. Conclusion

In this paper, a design of chiral-lattice-based elastic EMM beam with multiple resonators is suggested for the broadband vibration suppression by utilizing their individual bandgaps. First, a theoretical vibration modeling of the EMM beam with multiple local resonators is implemented based on the TBT model. To achieve broadband vibration attenuation, an EMM beam with distributed section resonators is suggested by eliminating dynamic interaction between different resonators and its resulting passbands. Attention is paid on quantitative determination of required unit number of the resonator to achieve desired vibration suppression. Finally, the chiral-lattice-based EMM beam is fabricated and experimental testing of the proposed structure is conducted to validate the design.

Acknowledgment

This work was supported in part by Air Force Office of Scientific Research under Grant no. AF 9550-10-0061 with Program Manager Dr. Byung-Lip (Les) Lee, and National Natural Science Foundation of China under Grant no. 10832002.

Appendix A. Effective bending stiffness and effective transverse shear stiffness of the homogenized sandwich beam

The finite sandwich beam consists of two face sheets which are made of Al and a core layer made of the chiral lattice, as shown in Fig. A1. The core layer can be represented by an effective isotropic medium with three effective material parameters: ρ_{eff}, E_{eff}, and υ_{eff} through the effective formulation approach [16]. With the equivalent core layer, all three layers in the sandwich beam are isotropic materials and the in plane stress–strain relation in each layer can be expressed as

$$\begin{Bmatrix} \sigma_x \\ \sigma_y \\ \sigma_{xy} \end{Bmatrix} = \begin{bmatrix} Q_{11} & Q_{12} & 0 \\ Q_{12} & Q_{11} & 0 \\ 0 & 0 & Q_{66} \end{bmatrix} \begin{Bmatrix} \varepsilon_x \\ \varepsilon_y \\ \varepsilon_{xy} \end{Bmatrix}, \tag{A.1}$$

where

$$Q_{11} = \frac{E(1-\upsilon)}{(1+\upsilon)(1-2\upsilon)}, \quad Q_{12} = \frac{E\upsilon}{(1+\upsilon)(1-2\upsilon)}, \quad \text{and} \quad Q_{66} = \frac{E}{2(1+\upsilon)}.$$

Integrating Eq. (A.1) through the thickness of the beam results in the following relation between the resultant forces and moments and the strains and curvatures:

$$\begin{Bmatrix} \mathbf{N} \\ \mathbf{M} \end{Bmatrix} = \begin{bmatrix} \mathbf{A} & \mathbf{B} \\ \mathbf{B} & \mathbf{D} \end{bmatrix} \begin{Bmatrix} \varepsilon \\ \kappa \end{Bmatrix}, \tag{A.2}$$

where **A** is the extensional stiffness matrix, **B** is the bending–extension coupling stiffness matrix and **D** is the bending stiffness matrix. Since the homogenized sandwich beam is symmetric with respect to the middle surface, the components in the bending–extension coupling stiffness matrix **B** are zero. The components of the bending stiffness matrix **D** for a

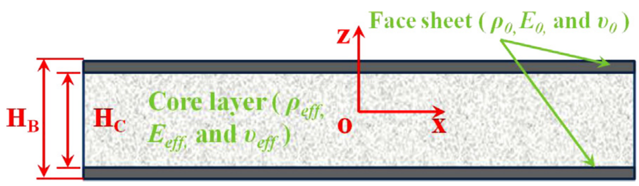

Fig. A1. The homogenized sandwich beam.

sandwich beam can be obtained as follows:

$$D_{11}=D_{22}=\frac{1}{12}\left[Q_{11}^{f}(H_B^3-H_C^3)+Q_{11}^{c}H_C^3\right],$$
$$D_{12}=\frac{1}{12}\left[Q_{12}^{f}(H_B^3-H_C^3)+Q_{12}^{c}H_C^3\right],$$
$$D_{66}=\frac{1}{12}\left[Q_{66}^{f}(H_B^3-H_C^3)+Q_{66}^{c}H_C^3\right]. \tag{A.3}$$

where the superscript 'f' and 'c' represent the face sheet and core layer, respectively. Then, the compliance equations can be obtained by inverting the matrices in Eq. (A.2),

$$\begin{Bmatrix}\varepsilon\\ \kappa\end{Bmatrix}=\begin{bmatrix}\alpha & 0\\ 0 & \delta\end{bmatrix}\begin{Bmatrix}\mathbf{N}\\ \mathbf{M}\end{Bmatrix}, \tag{A.4}$$

where

$$\delta_{11}=\delta_{22}=\frac{D_{11}}{(D_{11}^2-D_{12}^2)},\quad \delta_{12}=\frac{-D_{12}}{(D_{11}^2-D_{12}^2)},\quad \delta_{66}=\frac{1}{D_{66}}. \tag{A.5}$$

Using the equilibrium equation for the stresses in xz plane in the absence of body forces and integrating through the thickness, the shear stress expression becomes

$$\sigma_{xz}=-\int_{-H_B/2}^{z}\sigma_{x,x}dz. \tag{A.6}$$

Considering only the resultant component in x direction, Q_x, then, $N_{x,x}=0$ and $M_{x,x}=-Q_x$. Substituting Eqs. (A.1) and (A.4) into (A.6) yields

$$\sigma_{xz}=-\int_{-H_B/2}^{z}Q_x z(Q_{11}\delta_{11}+Q_{12}\delta_{12})dz. \tag{A.7}$$

Notice that the constitutive relations for transverse shear stresses are

$$\begin{Bmatrix}\sigma_{xz}\\ \sigma_{yz}\end{Bmatrix}=\begin{bmatrix}Q_{55} & 0\\ 0 & Q_{44}\end{bmatrix}\begin{Bmatrix}\gamma_{xz}\\ \gamma_{yz}\end{Bmatrix}. \tag{A.8}$$

The shear strain energy per unit length can be obtained as

$$U=\frac{W_B}{2}\int_{-H_B/2}^{H_B/2}\frac{\sigma_{xz}^2}{Q_{55}}dz=\frac{W_B}{2}\int_{-H_B/2}^{H_B/2}\frac{Q_x^2}{Q_{55}}\left[\int_{-H_B/2}^{z}z(Q_{11}\delta_{11}+Q_{12}\delta_{12})dz\right]^2dz, \tag{A.9}$$

where W_B is the width of the beam. For the sandwich beam consisting of two face sheets and a core layer, the shear strain energy can be rewritten according to the materials of each layer in the sandwich beam:

$$U=\frac{W_B}{2}\left\{\int_{-H_B/2}^{-H_C/2}\frac{Q_x^2}{Q_{55}^f}\left[\int_{-H_B/2}^{z}z(Q_{11}^f\delta_{11}+Q_{12}^f\delta_{12})dz\right]^2dz+\int_{H_C/2}^{H_B/2}\frac{Q_x^2}{Q_{55}^f}\left[\int_{-H_B/2}^{z}z(Q_{11}^f\delta_{11}+Q_{12}^f\delta_{12})dz\right]^2dz\right.$$
$$\left.+\int_{-H_C/2}^{H_C/2}\frac{Q_x^2}{Q_{55}^c}\left[\int_{-H_B/2}^{-H_C/2}z(Q_{11}^f\delta_{11}+Q_{12}^f\delta_{12})dz+\int_{-H_C/2}^{z}z(Q_{11}^c\delta_{11}+Q_{12}^c\delta_{12})dz\right]^2dz\right\}. \tag{A.10}$$

Assuming a constant transverse shear strain through the beam thickness, the constitute relation for the transverse shear resultant can be rewritten as

$$Q_x=(kG\overline{A})\gamma_{xz}, \tag{A.11}$$

where $(kG\overline{A})$ is the effective transverse shear stiffness. Thus, using Eq. (A.11), we can obtain an alternative form of shear strain energy:

$$U=\frac{1}{2}\frac{Q_x^2}{(kG\overline{A})}. \tag{A.12}$$

By equating the strain energy given by Eqs. (A.10) and (A.12), the effective transverse shear stiffness can be expressed as a function of the materials properties of each layer in the sandwich beam:

$$(kG\overline{A})=W_B\left\{\int_{-H_B/2}^{-H_C/2}\frac{1}{Q_{55}^f}\left[\int_{-H_B/2}^{z}z(Q_{11}^f\delta_{11}+Q_{12}^f\delta_{12})dz\right]^2dz+\int_{H_C/2}^{H_B/2}\frac{1}{Q_{55}^f}\left[\int_{-\frac{H_B}{2}}^{z}z(Q_{11}^f\delta_{11}+Q_{12}^f\delta_{12})dz\right]^2dz\right.$$
$$\left.+\int_{-H_C/2}^{H_C/2}\frac{1}{Q_{55}^c}\left[\int_{-H_B/2}^{-H_C/2}z(Q_{11}^f\delta_{11}+Q_{12}^f\delta_{12})dz+\int_{-H_C/2}^{z}z(Q_{11}^c\delta_{11}+Q_{12}^c\delta_{12})dz\right]^2dz\right\}^{-1}. \tag{A.13}$$

In order to obtain the effective bending stiffness from Eq. (A.4), in accordance with the assumption by Whitney et al. [26], only N_x and M_x are retained. Hence, the compliance matrix in Eq. (A.4) can be simplified as

$$\begin{Bmatrix} \varepsilon_x \\ \kappa_x \end{Bmatrix} = \begin{bmatrix} \alpha_{11} & 0 \\ 0 & \delta_{11} \end{bmatrix} \begin{Bmatrix} N_x \\ M_x \end{Bmatrix}, \tag{A.14}$$

and the expression for the force resultant of the sandwich can be obtained by inverting Eq. (A.14),

$$\begin{Bmatrix} N_x \\ M_x \end{Bmatrix} = \begin{bmatrix} \overline{\overline{A}} & 0 \\ 0 & \overline{\overline{D}} \end{bmatrix} \begin{Bmatrix} \varepsilon_x \\ \kappa_x \end{Bmatrix}, \tag{A.15}$$

where $\overline{\overline{A}} = (A_{11}A_{22} - A_{12}^2)/A_{22}$ and $\overline{\overline{D}} = 1/\delta_{11} = (D_{11}D_{22} - D_{12}^2)/D_{22}$. A_{ij} and D_{ij} $(i, j = 1, 2)$ are the components of the extensional stiffness matrix and the bending stiffness matrix, respectively. Therefore, the effective bending stiffness can be obtained as

$$(EI) = W_B \overline{\overline{D}} = \frac{W_B(D_{11}D_{22} - D_{12}^2)}{D_{22}}. \tag{A.16}$$

Reference

[1] Z.Y. Liu, X.X. Zhang, Y.W. Mao, Y.Y. Zhu, Z.Y. Yang, C.T. Chan, P. Sheng, Locally resonant sonic materials, *Science* 289 (2000) 1734–1736.
[2] Z.Y. Liu, C.T. Chan, P. Sheng, Analytic model of phononic crystals with local resonances, *Physical Review B* 71 (2005) 014103.
[3] G.W. Milton, J.R. Willis, On modification of Newton's second law and linear continuum elastodynamics, *Proceedings of the Royal Society A* 463 (2007) 855–880.
[4] R. Zhu, G.L. Huang, G.K. Hu, Effective dynamic properties and multi-resonant design of acoustic metamaterials, *ASME Journal of Vibration and Acoustics* 134 (2012) 031006.
[5] H.H. Huang, C.T. Sun, G.L. Huang, On the negative effective mass density in acoustic metamaterials, *International Journal of Engineering Science* 47 (2009) 610.
[6] J. Wen, G. Wang, D. Yu, H. Zhao, Y. Liu, Theoretical and experimental investigation of flexural wave propagation in straight beams with periodic structures: application to a vibration isolation structure, *Journal of Applied Physics* 97 (2005) 114907.
[7] L. Liu, M.I. Hussein, Wave motion in periodic flexural beams and characterization of the transition between Bragg scattering and local resonance, *ASME Journal of Applied Mechanics* 79 (2012) 011003.
[8] R. Zhu, G.L. Huang, H.H. Huang, C.T. Sun, Experimental and numerical study of guided wave propagation in a thin metamaterial plate, *Physics Letters A* 375 (2011) 2863–2867.
[9] Y. Xiao, J.H. Wen, X.S. Wen, Longitudinal wave band gaps in metamaterial-based elastic rods containing multi-degree-of-freedom resonators, *New Journal of Physics* 14 (2012) 033042.
[10] D. Yu, J.H. Wen, H. Zhao, Y.Z. Liu, X.S. Wen, Flexural vibration band gap in a periodic fluid-conveying pipe system based on the Timoshenko beam theory, *ASME Journal of Vibration and Acoustics* 133 (2011) 014502.
[11] J.S. Chen, B. Sharma, C.T. Sun, Dynamic behavior of sandwich structure containing spring-mass resonators, *Composite Structures* 93 (2011) 2120–2125.
[12] G.L. Huang, C.T. Sun, Band gaps in a multiresonator acoustic metamaterial, *ASME Journal of Vibration and Acoustics* 132 (2010) 031003.
[13] P.F. Pai, Metamaterial-based broadband elastic wave absorber, *Journal of Intelligent Material Systems and Structures* 21 (2010) 517–528.
[14] H.W. Sun, X.W. Du, P.F. Pai, Theory of metamaterial beams for broadband vibration absorption, *Journal of Intelligent Material Systems and Structures* 21 (2010) 1085–1101.
[15] Y. Xiao, J. Wen, X. Wen, Broadband locally resonant beams containing multiple periodic arrays of attached resonators, *Physics Letters A* 376 (2012) 1384–1390.
[16] X.N. Liu, G.K. Hu, G.L. Huang, C.T. Sun, Wave propagation characterization and design of two-dimensional elastic chiral metacomposite, *Journal of Sound Vibration* 330 (2011) 2536–2553.
[17] D. Yu, Y. Liu, G. Wang, H. Zhao, J. Qiu, Flexural vibration band gaps in Timoshenko beams with locally resonant structures, *Journal of Applied Physics* 100 (2006) 124901.
[18] A. Díaz-de-Anda, A. Pimentel, J. Flores, A. Morales, L. Gutiérrez, R.A. Méndez-Sánchez, *Journal of the Acoustical Society of America* 117 (2005) 281–2819.
[19] R.A. Méndez-Sánchez, A. Morales, J. Flores, Experimental check on the accuracy of Timoshenko's beam theory, *Journal of Sound Vibration* 279 (2005) 508–512.
[20] F. Romeo, A. Luongo, Invariant representation of propagation properties for bi-coupled periodic structures, *Journal of Sound Vibration* 257 (2002) 869–886.
[21] J.S. Jensen, Phononic band gaps and vibrations in one- and two-dimensional mass-spring structures, *Journal of Sound Vibration* 266 (2003) 1053–1078.
[22] Y. Liu, D. Yu, L. Li, H. Zhao, J. Wen, X. Wen, Design guidelines for flexural wave attenuation of slender beams with local resonators, *Physics Letters A* 362 (2007) 344–347.
[23] C.T. Sun, B.J. Kim, J.L. Bogdanoff, On the derivation of equivalent simple models for beam- and plate-like structures in dynamic analysis, *AIAA Dynamics Specialists Conference*, 1981, p. 523.
[24] A.P. Liu, R. Zhu, X.N. Liu, G.K. Hu, G.L. Huang, Multi-displacement microstructure continuum modeling of anisotropic elastic metamaterials, *Wave Motion* 49 (2012) 411–426.
[25] D. Yu, Y. Liu, H. Zhao, G. Wang, J. Qiu, Flexural vibration band gaps in Euler–Bernoulli beams with locally resonant structures with two degrees of freedom, *Physical Review B* 73 (2006) 064301.
[26] J.M. Whitney, C.E. Browning, A. Mair, Analysis of the flexure test for laminated composite materials, *ASTM Composite Materials: Testing and Design (Third Conference)*, 1974, pp. 30–45.